PDF Calculations of Turbulent Nonpremixed Flames of H_2 / CO_2 Using Reduced Chemical Mechanisms

S. TAING and A. R. MASRI
Department of Mechanical Engineering, The University of Sydney, NSW 2006, Australia

S. B. POPE
Sibley School of Mechanical and Aerospace Engineering, Cornell University, Ithaca, NY

A three-step chemical kinetic scheme, reduced systematically from a more detailed mechanism is used to represent chemical reaction in the Monte Carlo calculations of the joint velocity-composition probability density function (pdf) for pilot-stabilized turbulent jet nonpremixed flames of H_2/CO_2 fuel mixtures. Flames with a range of fuel jet velocities and hence varying degrees of finite rate chemical kinetic effects have been calculated. The independent variables used are mixture fraction, ξ and the specific molar abundance of three reactive scalars, Γ_{H_2O}, Γ_{CO_2}, and Γ_H. Three multidimensional look-up tables are generated for density, other dependent properties and the composition increments due to chemical reaction. The use of these tables in all subsequent calculations is computationally efficient. Terms representing the effects of pressure fluctuations, mechanical dissipation, and scalar dissipation are modeled using an improved particle interaction model. Solutions are obtained on a Sun-Sparc1 station using 30 000 Monte Carlo particles for the low jet velocity flames and this number is increased to 50 000 at high jet velocities. The calculated velocity and turbulence fields as well as centerline velocity decay rates have not been compared with measurements but are consistent with recent experimental data collected in similar piloted jet flames of methane fuel. The calculated mixing field compares well with experimental data and the calculated flame length is slightly shorter than the observed visible flame length. For the low- and intermediate-velocity flames, the calculated temperature and mass fractions of the stable species agree reasonably well with instantaneous experimental data collected in similar flames. At high jet velocities, when the flames are close to blowoff and the finite rate chemical kinetic effects are very significant, discrepancies occur between measurements and computations and the blowoff jet velocity is underpredicted by about 20%.

INTRODUCTION

Computing the structure of turbulent reacting flows where the finite rate chemical kinetic effects are substantial is a challenging and outstanding problem of combustion science. The nonlinearity of the reaction source term with temperature makes the applicability of gradient closure methods extremely difficult, if not impossible. Three main approaches to tackling this problem have recently gained prominence and show promising success but still require further development. These are the laminar flamelet approach, the probability density function (pdf) Monte Carlo method, and the conditional moment closure method. Each of these approaches still has some significant limitations and is currently subject to intense research.

The laminar flamelet approach to the modeling of turbulent nonpremixed flames was pioneered by Liew et al. [1]. The initial development of the concept treated the turbulent flame as an assembly of laminar flamelets controlled by the mixture fraction, ξ. A second variable, namely scalar dissipation rate, χ was introduced by Peters [2] to account for the effects of varying strain rates. A fluid sample representing a laminar flamelet may extinguish locally if its scalar dissipation rate, χ exceeds a quenching limit, χ_q determined by the laminar flamelet calculations. Such an approach does not allow for the presence of partially burned (or partially mixed) fluid samples that are observed experimentally in pilot-stabilized turbulent nonpremixed flames close to blowoff [3]. To account for this effect, Rogg et al. [4] introduced a third parameter to the model, namely a partial premixedness parameter, γ, and libraries of flamelets are then generated

0010-2180/93/$6.00

with respect to three variables (ξ, χ, γ). Such a modification still does not account for the peak levels of OH, CO, and H_2 observed experimentally, which exceed those calculated by steady laminar flamelets. Peters and co-workers [5] have shown that transient processes like ignition phenomena could lead to excessive levels of CO and H_2 in the calculated laminar flamelets. This led to another recent modification to the flamelet approach and the introduction of another parameter to account for transient effects [5].

The pdf Monte Carlo approach has mainly been developed by Pope [6–8], who solved the combined velocity-composition pdf transport equation for turbulent reacting jets using the Monte Carlo method. At a particular point in space and time the joint pdf $f(V, \psi; x, t)$ contains all the statistical information about the velocity and species concentration fields. Chemical reaction is represented exactly, but the mechanical and scalar dissipation as well as the effects of fluctuating pressure gradient need to be modeled. Chen et al. [9] have solved the composition pdf only using the standard κ–ϵ turbulence model to calculate the flowfield. They have used reduced chemical kinetics to calculate, with moderate success, the structure of pilot-stabilized flames of $CO/H_2/N_2$ [10] and CH_4 [9] at various turbulent mixing rates. More recently, Pope and Chen [11] solved the joint velocity-composition-dissipation equation using the Monte Carlo method. With such an approach, modeling is required only for the pressure fluctuation and scalar dissipation. The latter, which represents molecular mixing, is the main problem confronting the pdf methods. Norris and Pope [12] have recently developed improved molecular mixing models but more work is still needed in this area. This is critical considering that with the pdf approach, chemical reaction appears in closed form and realistic reduced chemistry can be represented in the turbulent flame computations.

A more recent development in this field is the conditional moment closure pioneered independently by Bilger [13] and Klimenko [14]. This approach is based on the experimental observation that the local temperature and composition in nonpremixed flames depend on the local mixture fraction and a reaction progress variable. Within a narrow mixture fraction range the reaction rate becomes linear with temperature, which may be a measure of the reaction progress. A balance equation is derived for the conditional averages of scalars where the conditioning is done with respect to mixture fraction, ξ. Initial results for CH_4 diffusion flames are promising [15]. A further extension of this approach is to doubly condition with respect to mixture fraction and a reaction progress variable.

Extensive experimental data have recently become available in well-characterized flames where the turbulence-chemistry interactions are significant. Pilot-stabilized flames of various fuels, in simple parabolic flows [16–20] as well as bluff-body stabilized flames with complex recirculating flows [21] have been investigated. It is essential to extend the current capabilities of the models to enable the calculation of these experimental data. Such extensive efforts are currently underway (5, 10, 13, 22). Correa and Pope [23] have recently attempted a calculation of recirculating flows using pdf Monte Carlo methods combined with finite volume techniques to calculate the velocity field.

The recent development of systematically reduced chemical kinetic schemes for various fuels and fuel mixtures is a great step forward in such efforts as it allows the incorporation of realistic chemistry in the calculations. The reduction methodology was pioneered by Peters [24] and Bilger et al. [25] and has more recently become the subject of regular international workshops [26]. The method is based on eliminating reactions that are very close to being in partial equilibrium and species that are in steady-state concentrations. A detailed account of reduced chemical kinetic mechanism for a range of fuels is presented in a book edited by Peters and Rogg [27]. More recently, Maas and Pope [28, 29] have developed a general procedure for simplifying chemical kinetic mechanisms based on the automatic identification and elimination of reactions with fast time scales. The method is referred to as the Intrinsic Low-Dimensional Manifolds (ILDM) method and it may, in principle, be automated to generate the reduced schemes as well as the

tables that will be used in the Monte Carlo pdf calculations.

The main objective of this article is to solve the transport equation for the joint velocity-composition pdf for pilot-stabilized turbulent nonpremixed flames of H_2/CO_2 fuels using a reduced three-step chemical kinetic mechanism. A five-dimensional look-up table is generated for the composition increments of three reactive scalars over a range of mixture fractions and reaction times. This fuel mixture is selected because of its broad reactive zone in mixture fraction space ($\Delta \xi_R \sim 0.5$). This makes the calculation less dependent on the adequacy of the mixing model since particles mixing from either side of the reactive zone are more likely to fall, when mixed, within the reactive zone due to its broad range. In an early attempt to calculate the structure of methane flames using a reduced four-step mechanism, capturing reacting particles was a problem due to the very narrow reactive zone. This fuel mixture is also of interest since CO_2 is not a passive diluent and it is converted to CO depending on the local conditions of the mixture. Calculations are compared with experimental measurements obtained in pilot-stabilized flames of similar fuel using the joint Raman–Rayleigh–Fluorescence technique.

EXPERIMENTAL DATA

Chemical kinetic effects in nonpremixed flames of H_2/CO_2 fuels have been investigated by Masri et al. [30]. In the experiment, a mixture of H_2 and CO_2 with a volumetric ratio of $H_2/CO_2 = 1.15$ was used. The stoichiometric mixture fraction is $\xi_s = 0.37$. The piloted burner developed at Sydney University has a jet nozzle diameter of 7.2 mm and an annulus diameter of 18 mm. The coflow air is maintained at $\overline{U}_0 = 15$ m/s and the burned pilot gas velocity at $\overline{U}_p = 10$ m/s. At these conditions the flame blows off at a jet velocity, $\overline{U}_{BO} = 265$ m/s. Table 1 shows the flames that have been investigated experimentally. The experimental data are presented in the form of scatter plots for T, CO, CO_2, H_2, H_2O, O_2, and OH plotted versus mixture fraction, ξ at $x/D_j = 6$ and 39. The visible flame length is about 60 to 70 fuel jet diameters regardless of the jet velocity. As the jet velocity increases, the flame becomes unstable and extinction occurs at 4–10 fuel jet diameters downstream of the nozzle exit plane. The flame is reignited further downstream with a "rumbling" noise generated from the reignition region. Further increase in the jet velocity causes the whole flame to blow off except for the pilot flame, which extends for about 3 fuel jet diameters from the nozzle exit plane. The average measured temperature in flame $V1$ is 1200 and 1620 K at $x/D_j = 6$ and 39, respectively. The scatter plots of temperature and major species mass fractions for flames $V1$ and $V2$ at $x/D_j = 6$ are qualitatively similar. The scatter plots from flame $V3$, which is very close to blowoff, are significantly different to those of flames $V1$ and $V2$, as the temperature and the mass fractions of O_2, H_2, and H_2O show a much broader scatter covering the whole region between the fully burned and the frozen limits.

TABLE 1

Characteristics of the Investigated Jet Diffusion Flames of H_2/CO_2

Flame	$\overline{U}_j$ (m/s)	H_2/CO_2 (by vol.)	$\overline{U}_j/\overline{U}_{BO}$ blowoff	Description
$V1$	130	1.15	0.49	stable
$V2$	229	1.15	0.86	stable
$V3$	260	1.15	0.98	unstable

MODELING

Joint Pdf Transport Equation

For low Mach number flows, the state of the fluid at any location can be fully described by the three components of velocity U and a set of σ scalar ϕ, where $\phi = \phi_1, \phi_2, \ldots, \phi_\sigma$. The pdf, $f(V, \psi; x, t)$ is the joint pdf of U and ϕ. In turbulent reactive flows, the joint pdf, $f(V, \psi; x, t)$ contains a complete one-point statistical description of velocity and composition. If $Q(U, \phi)$ is a function of U and ϕ which corresponds to $Q(V, \psi)$, where $Q(V, \psi)$ is a function defined everywhere in velocity and composition space, then the mean value of Q is

$$\overline{Q}(U, \phi) = \iint Q(V, \psi) f(V, \psi) dv\, d\psi,$$

where $\int\int dV\, d\psi$ is the integral over the whole space. Full details of the joint pdf transport equation and its derivation may be found in Pope [31]. The transport equation for the joint pdf $f(V, \psi; x, t)$ is given by

$$\rho(\psi)\frac{\partial f}{\partial t} + \rho(\psi)V_j\frac{\partial f}{\partial x_i} + \left(\rho(\psi)g_j - \frac{\partial \bar{p}}{\partial x_j}\right)\frac{\partial f}{\partial V_j} + \frac{\partial}{\partial \psi_\alpha}[\rho(\psi)S_\alpha(\psi)f] = \frac{\partial}{\partial V_j}\left[\left(\overline{-\frac{\partial \tau_{i,j}}{\partial x_j} + \frac{\partial p'}{\partial x_j}\middle| V, \psi}\right)f\right] + \frac{\partial}{\partial \psi_\alpha}\left[\left(\overline{-\frac{\partial J_i^\alpha}{\partial x_i}\middle| V, \psi}\right)f\right]. \quad (1)$$

In the above equation $\bar{p}$ and p' are the mean and fluctuating pressure; g_j is the body force (per unit mass) in the x_j direction; S_α is the mass rate of addition (per unit mass) of species α due to reaction; τ_{ij} is the sum of the viscous and viscous-diffusive stress tensors; and J_i^α is the diffusive mass flux of species α in x_i direction. The mean pressure $\bar{p}$ can be calculated from a separate equation described by Pope [31], and the density $\rho(\psi)$ and $S_\alpha(\psi)$ are known functions. Thus the terms on the left-hand side are in closed form, while the terms τ_{ij}, p', and J_i^α on the right-hand side need to be modeled.

In this paper, one conserved scalar, ξ, and three reactive scalars ($\Gamma_{CO_2}, \Gamma_{H_2O}, \Gamma_H$) are used in the pdf calculations along with three components of velocity, V. Here $\Gamma_i = Y_i/W_i$, where Y_i is the mass fraction of species i and W_i is the molecular weight. One point statistics of these dependent variables are functions of the axial and the radial coordinates, x and r only. Because the flow is statistically axisymetric and stationary, it is not dependent on time, t, and on the circumferential coordinate. All other thermochemical quantities are function of ϕ ($\phi = \xi, \Gamma_{CO_2}, \Gamma_{H_2O}, \Gamma_H$) and can be determined from the joint pdf $f(V, \psi; x, r)$. The mean density is

$$\bar{\rho}(x, r) = \int\int \rho(\psi) f(V, \psi; x, r)\, dV\, d\psi. \quad (2)$$

where V and ψ are the independent velocity and composition variables. The terms on the right-hand side of the pdf transport equation, Eq. 1, are modeled conditionally by treating turbulent and nonturbulent particles separately based on mixture fraction ξ. This is described in more detail by Pope [31].

For conditional modeling, a constant is assigned to each of the three processes that describe the interactions between turbulent and nonturbulent fluid. These are $C_g = 1.5$, $C_m = 1.5$, and $C_e = 5.0$ for entrainment, momentum exchange, and energy exchange, respectively. For the turbulent particles, the turbulent kinetic energy dissipation is modeled by the improved stochastic mixing model [32] with constant $C_R = 4.5$. Scalar dissipation is also accounted for by using an improved stochastic mixing model [33] which is similar to that used for turbulent kinetic energy but with a constant $C_\phi = 2.0$ being the ratio of the velocity to scalar time scales. The model allows for correlated mixing in velocity and composition space and the constant $C_{u\phi} = 1.0$ is used to define the degree of correlation [31].

The joint pdf $f(V, \psi; x, t)$ contains no information about the time or length scales of the turbulent fluctuations, so this information must be supplied. Masri and Pope [36] have used a new model for turbulent mixing frequency, ω:

$$\omega = C_\omega \int_0^\infty \left(\frac{\partial \bar{u}}{\partial r}\right)^2 dr \Big/ \int_0^\infty \left(\left|\frac{\partial \bar{u}}{\partial r}\right|\right) dr, \quad (3)$$

where C_ω is a constant. Equation 3 is appropriate for this flame geometry as it does account for the shear layers on the fuel and air sides of the pilot stream. In calculating the structure of pilot-stabilized turbulent nonpremixed flames of methane [36], a value of $C_\omega = 0.3$ was used, as this gave the best agreement with the experimental data for both the velocity and mixing fields. It is essential that the same value of $C_\omega = 0.3$ be used in the present calculations since the same piloted flame geometry is used.

THREE-STEP REDUCED MECHANISM

The development of reduced reaction mechanisms for complex combustion systems has made the prediction of turbulent reacting flows using pdf methods possible. Earlier, simplified reaction mechanisms were largely based on curve fits of limited experimental data. The recently developed mechanisms are systematically reduced from complex chemical kinetic schemes using steady-state and partial equilibrium assumptions [24–27].

Using the skeletal reaction mechanism shown in Table 2, Rogg and Williams [35] derived a three-step reduced mechanism to model premixed, wet CO flames. By applying the steady state assumption to HCO and HO_2, and assuming the reactions $H_2 + O \leftrightarrow OH + H$(R3) and $H_2 + OH \leftrightarrow H_2O + H$(R5) to be equilibrated, the following three-step mechanism is obtained.

$$CO + H_2O \leftrightarrow CO_2 + H_2, \quad \text{(I)}$$

$$2H + M \rightarrow H_2 + M, \quad \text{(II)}$$

$$O_2 + 3H_2 \leftrightarrow 2H + 2H_2O. \quad \text{(III)}$$

The global reaction rates can be expressed in terms of elementary reaction rates as follows:

$$\omega_{\mathrm{I}} \approx \omega_{38}, \quad (f, b)$$

$$\omega_{\mathrm{II}} \approx \omega_{15} + \omega_{46}, \quad (f, f)$$

$$\omega_{\mathrm{III}} \approx \omega_{1}, \quad (f, b)$$

where ω_i is the net forward rate for reaction i and subscripts f and b refer to forward and backward rates, respectively. Chen et al. [10] used the same reduced mechanism to calculate the structure of $CO/H_2/N_2$ nonpremixed flames. They reported that the partial equilibrium assumption for R3 was inadequate and proposed a steady state assumption for [O] giving a much better representation over a broader range of ξ and stretch rates. The formulation developed by Chen et al. [10] is adopted in this paper:

Assuming partial equilibrium for R5 yields

$$[\mathrm{OH}] = \frac{K_{5b}[\mathrm{H_2Q}][\mathrm{H}]}{K_{5f}[\mathrm{H_2}]}.$$

Assuming steady state for HCO and O gives

$$[\mathrm{HCO}] = \frac{K_{57f}[\mathrm{CO}][\mathrm{H}][\mathrm{M}]}{K_{57b}[\mathrm{M}] + K_{46f}[\mathrm{H}]},$$

$$[\mathrm{O}] = \frac{K_{1f}[\mathrm{O_2}][\mathrm{H}] + K_{3b}[\mathrm{OH}][\mathrm{H}] + K_{7f}[\mathrm{OH}]^2}{K_{1b}[\mathrm{OH}] + K_{3f}[\mathrm{H_2}] + K_{7b}[\mathrm{H_2O}]}$$

TABLE 2

Short Mechanism for $CO/H_2/N_2$ Flames[a]

Reaction	*Aj*	*bj*	*Ej*	
$O_2 + H \leftrightarrow OH + O$	2.00×10^{14}	0.00	70.30	(R1)
$H_2 + O \leftrightarrow OH + H$	5.06×10^{4}	2.67	26.30	(R3)
$H_2 + OH \leftrightarrow H_2O + H$	1.00×10^{8}	1.60	13.80	(R5)
$OH + OH \leftrightarrow H_2O + H$	1.50×10^{9}	1.14	0.42	(R7)
$H + H + M \rightarrow H_2 + M$	1.80×10^{18}	−1.00	0.00	(R9)
$H + OH + M \rightarrow H_2O + M$	2.20×10^{22}	−2.00	0.00	(R11)
$H + O_2 + M \rightarrow HO_2 + M$	2.30×10^{18}	−0.80	0.00	(R15)
$HO_2 + H \rightarrow OH + OH$	1.50×10^{14}	0.00	4.20	(R17)
$HO_2 + H \rightarrow H_2 + O_2$	2.50×10^{13}	0.00	2.90	(R19)
$HO_2 + H \rightarrow H_2O + O$	3.00×10^{13}	0.00	7.20	(R21)
$HO_2 + O \rightarrow OH + O_2$	1.80×10^{13}	0.00	−1.70	(R23)
$HO_2 + OH \rightarrow H_2O + O_2$	6.00×10^{13}	0.00	0.00	(R25)
$CO + OH \leftrightarrow CO_2 + H$	4.40×10^{6}	1.50	−3.10	(R38)
$HCO + H \rightarrow CO + H_2$	2.00×10^{14}	0.00	0.00	(R46)
$CO + H + M \leftrightarrow HCO + M$	1.14×10^{15}	0.00	9.98	(R57)

[a] Here the rate constant for the jth reaction is given by $k_j = A_j T^{bj} \exp[-E_j/(RT)]$, and the coefficients A_j, b_j, and E_j with units in cm, mole KJ, and K. Third-body collision efficiencies, Z_i, relative to H_2 are taken from Warnatz [34] as $Z_H = 1$, $Z_{O_2} = 0.4$, $Z_{N_2} = 0.4$, $Z_{H_2O} = 6.5$, $Z_{Ar} = 0.35$. The reaction numbers correspond to those in a *full* mechanism from which Rogg and Williams [35] developed this short mechanism.

Considering steady state for HO_2, and the result is

$$[HO_2] = \frac{K_{15f}[H][O_2][M]}{K_{25f}[OH] + K_{23f}[O] + (K_{17f} + K_{19f} + K_{21f})[H]},$$

which can be approximated by

$$[HO_2] = \frac{K_{15f}[H][O_2][M]}{K_{25f}[OH]}.$$

TABULATION PROCEDURE

A total of six reactive scalars are involved in the computations using the three-step reduced mechanism. These are CO, CO_2, H_2, H_2O, O_2, and H. In this section, it is shown that three species have to be taken as independent variables and the remaining three can then be calculated using three equations for mixture fraction generated using the principle of conservation of C, H, and O atoms and the assumption that differential diffusion effects are negligible. The mixture fraction, ξ is defined as

$$\xi = \frac{\beta_i - \beta_{i,0}}{\beta_{i,j} - \beta_{i,0}},$$

where β_i is the mass fraction of the element i, and subscripts 0 and j refer to the coflow air stream and the fuel stream at the jet exit plane, respectively. At the jet exit plane, ξ is zero in the oxidant stream and unity in the fuel stream. The fuel used is a mixture of 53.5% of H_2 and 46.5% CO_2 (by volume), which gives a stoichiometric mixture fraction, $\xi_s = 0.37$. The mass fractions of C, O, and H atoms are conserved and are expressed as follows:

$$\beta_C = W_C(\Gamma_{CO} + \Gamma_{CO_2}),$$

$$\beta_O = W_O(\Gamma_{CO} + 2\Gamma_{CO_2} + \Gamma_{H_2O} + 2\Gamma_{O_2}),$$

$$\beta_H = W_H\big(\Gamma_H + 2(\Gamma_{H_2} + \Gamma_{H_2O})\big).$$

For this fuel mixture, $\Gamma_{CO_2,J} = 0.0216$, $\Gamma_{H_2,J} = 0.025$, and

$$\beta_{C,0} = 0,$$

$$\beta_{O,0} = \alpha, \quad \text{where } \alpha = Y_{O_2,0} = 0.233,$$

$$\beta_{H,0} = 0,$$

$$\beta_{C,J} = W_C\Gamma_{CO_2,J},$$

$$\beta_{H,J} = 2W_H\Gamma_{H_2,J},$$

$$\beta_{O,J} = 2W_O\Gamma_{CO_2,J}.$$

The mixture fraction calculated with respect to conserved scalars β_C, β_O, and β_H is represented as

$$\xi_C = \frac{\beta_C - \beta_{C,0}}{\beta_{C,J} - \beta_{C,0}} = \frac{\beta_C}{W_C\Gamma_{CO_2,J}}$$

$$= \frac{W_C}{W_C\Gamma_{CO_2,J}}(\Gamma_{CO} + \Gamma_{CO_2}), \tag{4}$$

$$\xi_O = \frac{W_O(\Gamma_{CO} + 2\Gamma_{CO_2} + \Gamma_{H_2O} + 2\Gamma_{O_2}) - \alpha}{2W_O\Gamma_{CO_2,J} - \alpha}, \tag{5}$$

$$\xi_H = \frac{W_H}{2W_H\Gamma_{H_2,J}}\big(\Gamma_H + 2(\Gamma_{H_2} + \Gamma_{H_2O})\big). \tag{6}$$

By disregarding differential diffusion effects, the mixture fraction calculated from Eqs. 4–6 are identical, and $\xi = \xi_C = \xi_O = \xi_H$. Equations 7–9 can be generated from Eqs. 4–6 as follows:

$$\xi\Gamma_{CO_2,J} = \Gamma_{CO} + \Gamma_{CO_2}, \tag{7}$$

$$2\xi\Gamma_{CO_2,J} + \frac{\alpha}{W_O}(1 - \xi)$$

$$= \Gamma_{CO} + 2\Gamma_{CO_2} + \Gamma_{H_2O} + 2\Gamma_{O_2}, \tag{8}$$

$$2\xi\Gamma_{H_2,J} = 2\Gamma_{H_2} + 2\Gamma_{H_2O} + \Gamma_H. \tag{9}$$

The reactive scalars selected as independent variables are Γ_{CO_2}, Γ_{H_2O}, and Γ_H. The remaining three scalars are determined from Eqs. 7–9.

Tabulation Strategy

At each step in the calculations, the density of each Monte Carlo particle and the change in

the compositions of each reactive particle due to chemical reaction has to be computed. The latter involves numerical integration over the reaction time for each particle and this process is computationally intensive. To reduce computational time, three look-up tables are used instead of direct calculations of density, specific molar abundance of dependent variables, and composition increments due to chemical reactions. The density and composition tables are produced for the full allowed space, which is determined by the atomic balance equations 7–9. The table for composition increments due to reaction is generated only for the reactive space, which covers a narrower mixture fraction range bounded by the upper and lower reactive limits, ξ_U and ξ_L, respectively. This is useful since it leads to a reduction in computer storage space and to an improved resolution in the tables. The upper and lower reactive limits for the fuel mixture are determined from separate calculations of the structure of laminar diffusion flames of H_2/CO_2 fuels using a detailed chemical kinetic scheme [30].

Thousands of table entries are generated for combinations of values for ξ, Γ_{CO_2}, Γ_{H_2O}, and Γ_H. The range of values covered for each scalar is determined sequentially following a tree diagram presented in Fig. 1. Each reactive scalar

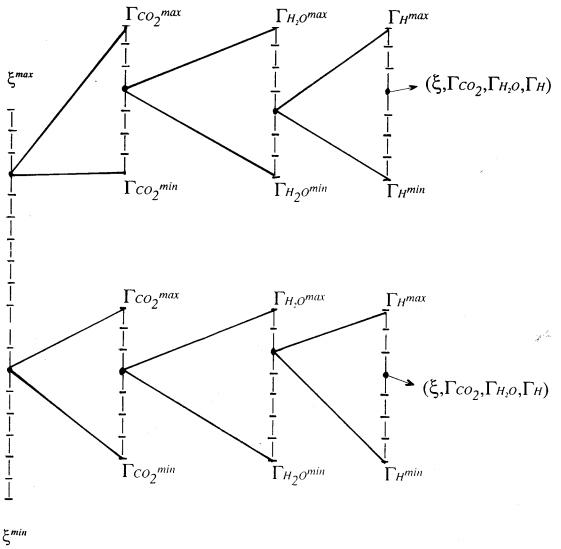

Fig. 1. Tree diagram followed in the sequential determination of tabulation nodes for $\xi, \Gamma_{CO_2}, \Gamma_{H_2O}, \Gamma_H$.

has a valid domain which is bounded by a minimum and maximum limit. First, the mixture fraction range is divided into a number of intervals and for each node within this interval maximum and minimum values of Γ_{CO_2} are determined. The valid domain for Γ_{CO_2} is in turn divided into intervals. For each node within this interval, and given ξ and Γ_{CO_2}, maximum and minimum values for Γ_{H_2O} are determined. The same sequence continues in order to generate a valid domain for Γ_H, which is subdivided into intervals and each node within this interval now has a complete set of values for ξ, Γ_{CO_2}, Γ_{H_2O}, and Γ_H. The actual bounds for each scalar are detailed in the next section for both allowed and reactive spaces.

The density and compositions tables are four dimensional in ξ, Γ_{CO_2}, Γ_{H_2O}, and Γ_H. At each node in the density table a single entry, namely density, is stored. Four entries are stored at each node in the composition table. These are the calculated values for T, Γ_{CO}, Γ_{O_2}, and Γ_{H_2}. The reactive table is five dimensional, where the fifth dimension is the reaction time. Each node in the table corresponds to set values for ξ, Γ_{CO_2}, Γ_{H_2O}, Γ_H, and Δt, where Δt is the reaction time interval. At each node in the table the integral $\int_0^{\Delta t}(d\Gamma_i/dt)\,dt$ is calculated for CO_2, H_2O, and H, respectively, using the corresponding rates for reactions I, II, and III. Three entries are stored at each node in the reaction table giving the change in composition due to chemical reaction over a time interval Δt.

The size of the tables is practically determined by the available memory storage space. The density and composition tables have dimensions $20 \times 8 \times 8 \times 8$ for ξ, Γ_{CO_2}, Γ_{H_2O}, and Γ_H, respectively. The table of composition increments due to chemical reaction has dimensions $20 \times 8 \times 8 \times 8 \times 10$, where the fifth dimension is for reaction time intervals. With three entries at each nodes, about 3×10^5 words are to be stored in the reaction table. During the Monte Carlo simulations, the scalar changes due to chemical reaction for each particle in the reactive space are obtained from the reaction table by an efficient multilinear interpolation scheme. Density and the specific molar abundance of each species in the allowed space are interpolated similarly.

Tabulation Limits

The minimum and maximum limits in both the reactive and allowed spaces are determined sequentially for each of the independent variables ξ, Γ_{CO_2}, Γ_{H_2O}, and Γ_H as follows:

(1) Mixture fraction ξ:

$$\textit{Reactive space} \quad \xi^{\min} = \xi_L = 0.1, \quad \xi^{\max} = \xi_U = 0.6.$$

$$\textit{Allowed space} \quad \xi^{\min} = 0.0, \quad \xi^{\max} = 1.0.$$

(2) The reactive and allowed mixture fraction spaces ($\xi^{\max} - \xi^{\min}$) are divided into a number of nodes. Given a value for ξ at any node, the maximum and minimum of Γ_{CO_2} for both the *reactive space* and the *allowed space* is obtained as follows:

$$\Gamma_{CO_2}{}^{\max} = \xi \Gamma_{CO_2,J}$$

$$\Gamma_{CO_2}{}^{\min} = 0.8\xi\Gamma_{CO_2,J} \quad \text{for } \xi \le 0.5,$$

$$= 0.8\Gamma_{CO_2,J}(1 - \xi) \quad \text{for } \xi > 0.5.$$

It is assumed here that a maximum of 20% of the carbon dioxide available may be converted to CO. This assumption is introduced to limit the tabulated domain for both CO and CO_2 to realistic values and hence maintain reasonable resolution in the tables. The assumption is supported by both experimental results as well as laminar flame calculations that show that not more than 20% of CO_2 is converted to CO regardless of the flame condition.

(3) The range: ($\Gamma_{CO_2}{}^{\max} - \Gamma_{CO_2}{}^{\min}$) is then divided into intervals. Given a value of ξ and Γ_{CO_2} at any node, upper and lower limits for Γ_{H_2O} are determined for the reactive space as follows:

$$\Gamma_{H_2O}{}^{\max I} = \Gamma_{CO_2,J}\xi - \Gamma_{CO_2} + \frac{\alpha}{W_O}(1 - \xi),$$

$$\Gamma_{H_2O}{}^{\max II} = \xi \Gamma_{H_2,J},$$

$$\Gamma_{H_2O}{}^{\max} = \min\left\{\Gamma_{H_2O}{}^{\max I}, \Gamma_{H_2O}{}^{\max II}\right\},$$

$$\Gamma_{H_2O}{}^{\min} = 0.3\Gamma_{H_2O}{}^{\max}.$$

To improve the resolution in the reactive domain, it is assumed here that in the reactive zone at least some of the hydrogen is converted to H_2O and the minimum value for Γ_{H_2O} is $0.3\Gamma_{H_2O}{}^{\max}$. This assumption is also supported by the experimental data and laminar flame calculations. In the allowed space, however, the possibility of no conversion of H_2 to H_2O is allowed and maximum and minimum values of Γ_{H_2O} are as follow:

$$\Gamma_{H_2O}{}^{\max} = \min\left\{\Gamma_{H_2O}{}^{\max I}, \Gamma_{H_2O}{}^{\max II}\right\},$$

$$\Gamma_{H_2O}{}^{\min} = 0.0.$$

(4) The range: ($\Gamma_{H_2O}{}^{\max} - \Gamma_{H_2O}{}^{\min}$) is then divided into intervals. Given values of ξ, Γ_{CO_2}, and Γ_{H_2O} the upper and lower limits of Γ_H can then be determined for both *reactive* and *allowed spaces*. It is assumed that a maximum of 5% of the H_2 available may be converted to H atoms to give $\Gamma_H{}^{\max}$ for the range of $0 < \xi \le 0.4$. This assumption is also justified from the laminar flame calculations.

$$\Gamma_H{}^{\max} = 0.05\xi\Gamma_{H_2,J}, \quad \text{for } \xi \le 0.4,$$

$$\Gamma_H{}^{\max} = 0.05\Gamma_{H_2,J}(0.4)\left(\frac{1 - \xi}{1 - 0.4}\right) \quad \text{for } \xi > 0.4,$$

$$\Gamma_H{}^{\min} = 0.0.$$

COMPUTATION PROCEDURE

The joint pdf transport equation is solved by the Monte Carlo method and the pdf is represented by a large number of stochastic particles, N. For a given flame, the initial conditions at $x = 0$ are generated and the solution is obtained by marching in the axial direction, x. The stochastic mixing, convection, mean pressure gradient, and reaction do not take place at $x = 0$. At each downstream step Δx, the density and compositions of each particle is obtained from the density and properties tables, respectively. The changes of the reactive scalars due to reaction are obtained from the reaction table.

The solution grid taken at the jet exit plane covers the pilot stream and part of the jet and air streams. This grid then expands toward the center of the jet and also outward as it moves downstream. The inner limit for the grid ex-

pansion is the jet centerline and the outer limit is $r/R_j = 7$. If a particle has a radial position, $r/R_j > 7.0$, then $\bar{u}$ is set to the coflow value and all other velocities including variances and covariances are set to zero.

Nguyen and Pope [37] have shown that the statistical error associated with a scalar decreases with the square root of the number of stochastic particles, N, and that the ensemble average converges to the true mean, $\overline{Q}(U, \phi)$, as N tends to infinity. It is important that a large enough number of stochastic particles are used in the computations to minimize the statistical error. This is limited by the available memory on the computer. The calculations here were repeated for the flame with $\overline{U}_j = 130$ m/s three times with $N = 10\,000$, 30 000, and 50 000, respectively. Calculations were also repeated for the flame with $\overline{U}_j = 190$ m/s with $N = 10\,000$, 30 000, 50 000, and 65 000. The calculated radial profiles for the mean temperature are plotted in Fig. 2 versus r/R_j for both flames with different values of N.

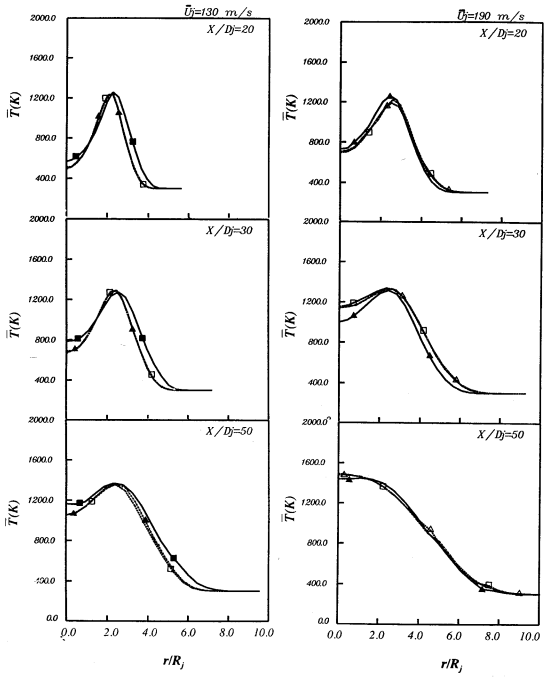

Fig. 2. Calculated radial profiles of mean temperature at various axial locations in two H_2/CO_2 flames with $\overline{U}_j$ = 130 m/s and $\overline{U}_j$ = 190 m/s with different values of Monte Carlo particles, N. Symbols, used here as line labels, refer to: ■: N = 10000; ▲: N = 30000; □: N = 50000; △: N = 65000.

For the flame with $\overline{U}_j = 130$ m/s, the radial and axial profiles for $N = 30\,000$ almost overlap with those of $N = 50\,000$. At $\overline{U}_j = 190$ m/s the deviation from $N = 30\,000$ to $N = 50\,000$ is quite apparent, but the profiles for $N = 50\,000$ almost overlap with those of $N = 65\,000$. For flames with high jet velocities where the chemical kinetic effects are significant, the larger number of particles is required to maintain a low statistical error. For the flames with $\overline{U}_j \leq 160$ m/s, 30 000 Monte Carlo particles are used in the computations while 50 000 particles are used for the flames with higher jet velocities. All the calculations are performed on a Sun-sparc1 station and are limited to $x/R_j \leq 200$. The required CPU times for flames with $\overline{U}_j = 130$ m/s and $\overline{U}_j = 190$ m/s are 1800 and 3000 min, respectively.

Initial Conditions

The normalized mean velocity and its rms of fluctuations as well as the mean mixture fraction profiles taken at the nozzle exit plane are shown in Fig. 3 for the flame with $\overline{U}_j = 80$ m/s. It should be noted that these initial conditions have not been directly measured but are approximated following a method established previously for similar piloted flames of methane fuel [36]. Fully developed turbulent pipe flow is considered in the main fuel jet such that the initial mean velocity profile yields a jet momentum and a mass flow rate that match the experimental conditions to within $\pm 2\%$. A similar procedure is followed for all other flames. Laminar flow with a uniform velocity profile is assumed at the pilot exit plane. This is justified by the low Reynolds number of ~ 250 in the exiting pilot stream. The velocity and turbulence profiles in the boundary layer of the coflowing stream are approximated from measurements taken in a similar configuration [36]. The mass and momentum of the coflow stream are to within $\pm 2\%$ of the experimental values. The coflow turbulent boundary layer extends to $r/R_j = 7.0$. The mean mixture fraction is $\bar{\xi} = 1.0$ at the fuel jet exit plane, $\bar{\xi} = \xi_s$ in the pilot, and $\bar{\xi} = 0$ in the coflow. The initial conditions for the remaining independent variables, namely Γ_{CO_2}, Γ_{H_2O}, and Γ_H are also specified. These

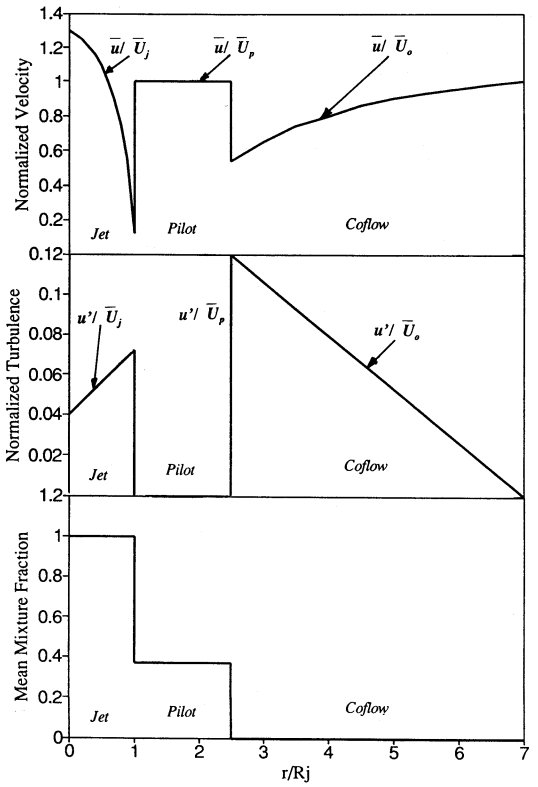

Fig. 3. Profiles of the normalized mean velocity, its rms of fluctuations and mean mixture fraction used at $x/D_j = 0$ as initial conditions for the flame with $\overline{U}_j = 80$ m/s.

reactive scalars remain, like ξ, uniform in each of the fuel jet, pilot and coflow exit planes. The following compositions are assigned to the particles at the jet exit plane according to their radial location:

	jet	*pilot*	*air*
$\overline{\xi}$	1.0	0.37	10^{-8}
$\overline{\Gamma}_{CO_2}$	0.0216	0.00735	10^{-8}
Γ_{H_2O}	10^{-8}	0.009	10^{-8}
$\overline{\Gamma}_H$	10^{-8}	0.0005	10^{-8}

Values of $\overline{\Gamma}_{CO_2}$, $\overline{\Gamma}_{H_2O}$, and $\overline{\Gamma}_H$ used in the pilot stream are obtained from separate calculations of the structure of a laminar flame with the same fuel composition as the pilot flame.

RESULTS AND DISCUSSION

Calculations are performed for a range of flames with different jet velocities but identical conditions at the pilot annulus exit plane. The jet velocities investigated are 80, 130, 160, 190, 210, and 220 m/s. At $\overline{U}_j = 80$ m/s, the flame is far from extinction and finite rate chemical kinetic effects are at a minimum. The experimental blowoff limit is approximately 265 m/s. The calculated blowoff jet velocity occurs at approximately 220 m/s, which is about 20% lower than the experimental value. The problems are essentially caused by the coarse particle interaction model that gives an unrealistic representation of molecular mixing. Due to this discrepancy, the experimental data for flames $V2$ and $V3$ (see Table 1) cannot be compared directly with calculated flames of similar jet velocities.

Flow Field and Mixing Field

Radial profiles of the mean and rms of fluctuations of velocity and mixture fraction are shown in Fig. 4 for the flame with $\overline{U}_j = 130$ m/s. Unfortunately there are no experimental data for the mean velocity, $\bar{u}$ and its rms of

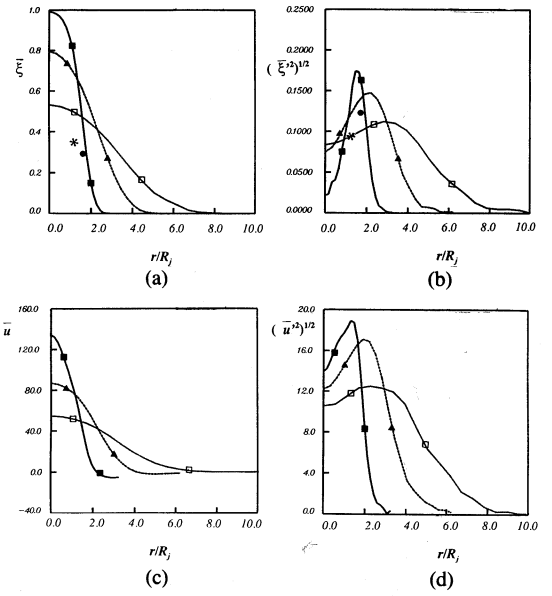

Fig. 4. Radial profiles of (a) mean mixture fraction, $\bar{\xi}$, and (b) its rms of fluctuations, $(\overline{\xi'^2})^{1/2}$ as well as (c) mean excess velocity, $\bar{u}$ and (d) its rms of fluctuations, $(\overline{U'^2})^{1/2}$ at $x/D_j = 6$, 20 and 39 in the flame with $\overline{U}_j = 130$ m/s. Symbols: ● and * refer to measurements at $x/D_j = 6$ and 39. Symbols ■, ▲, and □ label the profiles which refer to calculations at $x/D_j = 6$, 20, and 39, respectively.

fluctuations, u', with which to compare these calculations. A single experimental data point is available for the mean mixture fraction, $\bar{\xi}$, and its rms of fluctuations, ξ', and this is shown in Fig. 4. At $x/D_j = 6$, the agreement with the experimental data is very good for both $\bar{\xi}$ and ξ'. However, at $x/D_j = 39$, the measured mean mixture fraction is lower, indicating stronger mixing and a shorter flame length. Part of this discrepancy may be due to a slight shift in the radial location where measurements are made. Similar results were obtained for methane-piloted flames [36] where the level of agreement between experimental data and calculated values of $\bar{\xi}$ is excellent upstream but deteriorates further downstream at $x/D_j > 30$. The radial rate of flame spread is similar to that observed experimentally. It is interesting to note that the velocity deficit, which is due to the momentum deficit caused by the boundary layer on the air coflow side, persists down to $x/D_j \approx 40$. For a given axial location, the peaks in the rms of fluctuations of velocity and mixture fraction occur approximately at the same radial location. This indicates that the turbulent shear layer and the turbulent mixing layers almost overlap. At $x/D_j = 6$, 20, and 39, the peak values of ξ' and u' occur at radial locations of $r/R_j = 1.4$, 2.0, and 2.6, which correspond to mean mixture fractions $\bar{\xi} = 0.5$, 0.46, and 0.35, respectively. This implies that, on average, the turbulent shear and mixing layers lie within the reactive zone of the flame at these axial locations.

Figures 5a and 5b show axial profiles of the calculated centerline values of the excess velocity ratio, $\bar{U}_c/\bar{U}_{cj}$, and the rms of fluctuations of velocity, $(\overline{u'^2})^{1/2}$, for a range of flames. The decay in the excess velocity for $x/D_j \leq 60$ is proportional to $(x/D_j)^{-1}$, which is consistent with experimental observations in pilot-stabilized flames of methane fuel [38]. For $x/D_j > 60$, the slope for the velocity decay deviates from -1 because at these downstream axial locations the mean velocity have decreased significantly and the turbulence levels as shown in Fig. 5b have also dropped. The peak in the centerline values of u' occur further upstream at $x/D_j < 20$ regardless of the flame's jet exit velocity. Figures 5c and 5d show axial profiles of the centerline values of the mean mixture

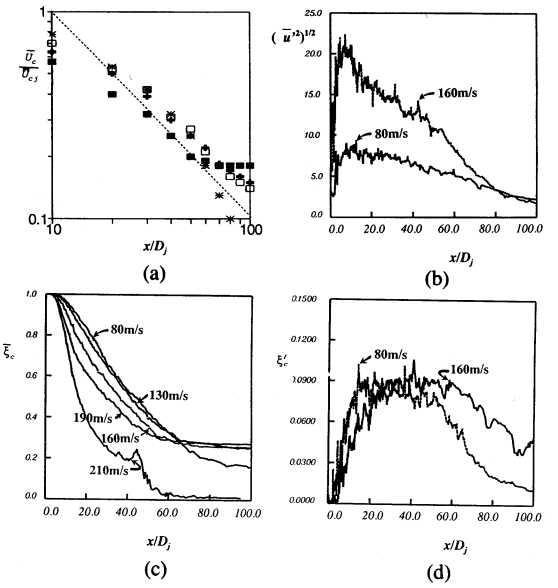

Fig. 5. Axial profiles of the calculated centerline values of the (a) excess velocity ratio $\bar{U}_c/\bar{U}_{cj}$ (b) rms of fluctuations of velocity $(\overline{u'^2})^{1/2}$ (c) mean mixture fraction, $\bar{\xi}$ and (d) its rms fluctuation $(\overline{\xi'^2})^{1/2}$ for a range of H_2/CO_2 flames. Symbols in plot (a) refer to calculations for: $*$: $\bar{U}_j = 80$ m/s; □: $\bar{U}_j = 130$ m/s; +: $\bar{U}_j = 160$ m/s; ■: $\bar{U}_j = 190$ m/s.

fraction, $\bar{\xi}_c$, and its rms of fluctuation, $(\overline{\xi_c'^2})^{1/2}$, for a range of flames. If the flame length is determined by the centerline location where $\bar{\xi}_c = \xi_s$, then the calculated flame length is $x/D_j = 58$ for the flames with $\bar{U}_j = 80$ and 130 m/s. The constant flame length with increasing mean jet velocity is consistent with experimental observations for fully developed turbulent jet flames [39]. For the higher jet velocity flames, the flame length decreases to $x/D_j =$ 50, 45, and 20 with $\bar{U}_j = 160$, 190, and 210 m/s, respectively. This decrease is due to the increasing proportion of unreacted fluid samples in the flame due to intense turbulent mixing rate. The flame with $\bar{U}_j = 210$ m/s is almost fully extinguished and close to a turbulent nonreacting jet. It should be noted that the flame length defined by $\bar{\xi}_c = \xi_s$ is shorter than the visible flame length, which is reported at $x/D_j \sim 70$, due to the turbulent flame brush which extends intermittently beyond the location where $\bar{\xi}_c = \xi_s$. The peak centerline values of ξ_c' shown in Fig. 5b occur at $x/D_j \sim 30$ regardless of the flame's jet exit velocity.

Slowly Mixing Flames

In this section, calculations are presented for two flames with $\bar{U}_j = 80$ and 130 m/s. The flames are at 35% and 60% of the calculated blowoff velocity and are, therefore, the least affected by finite rate chemical kinetics. Figure 6 shows six scatter plots for temperature versus mixture fraction at $x/D_j = 2$, 6, 10, 20, 39, and 50 calculated for the flame with $\bar{U}_j = 80$ m/s. At $x/D_j = 2$, the jet is still mainly influenced by the pilot gases and fluid particles lie along almost straight lines joining the pilot gas temperature to the temperature of the fuel and air streams, respectively. It should be noted that this does not necessarily indicate that fluid samples are fully reacted in this region. Close to the jet exit plane, the pilot stream separates the air and fuel streams and mixing occurs mainly between fluid particles from the pilot and fluid particles from the air or fuel streams resulting in the behavior obtained at $x/D_j = 2$. At $x/D_j = 6$ the peak temperature decreases to about 1400 K and some fluid samples within the reactive zone ($0.15 < \xi < 0.6$) have temperatures as low as 900 K. It is important to note that these low-temperature fluid samples are not locally extinguished because they have never been ignited in the first place. They result from mixing events between particles from the lean and rich side of stoichiometric. At $x/D_j = 10$, fluid samples are more fully reacted and the peak temperature increases to ~ 1500 K with only very few samples in the region around stoichiometric having temperatures below 1200 K. The peak temperature increases further to 1600 K at $x/D_j = 20$ and peak at this level for $x/D_j > 20$, this being the theoretical maximum determined by equilibrium. At $x/D_j = 39$ the flame is fully reacted with almost all fluid samples around $\xi = \xi_s$ having temperatures in the range 1300–1600 K.

Figure 7 shows radial profiles of mean temperature and the mass fractions of H, H_2, H_2O, CO, and CO_2 calculated at various axial

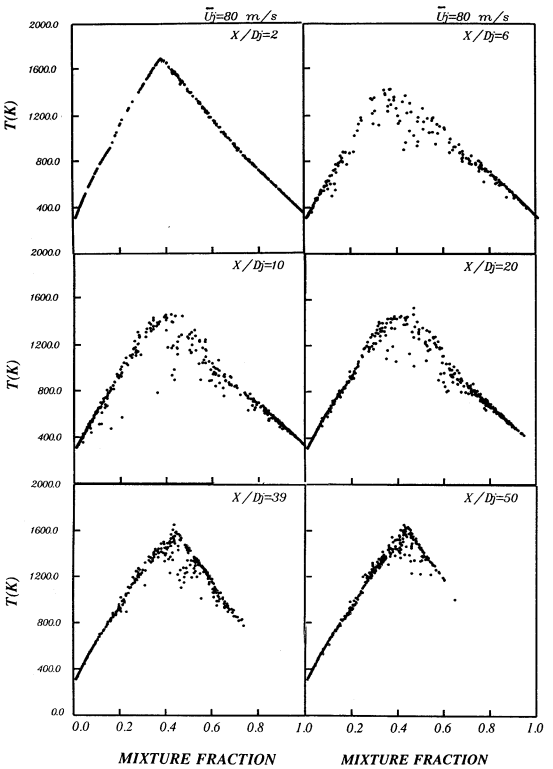

Fig. 6. Calculated scatter plots of temperature versus mixture fraction at various axial locations in a H_2/CO_2 piloted jet flame with $\bar{U}_j = 80$ m/s.

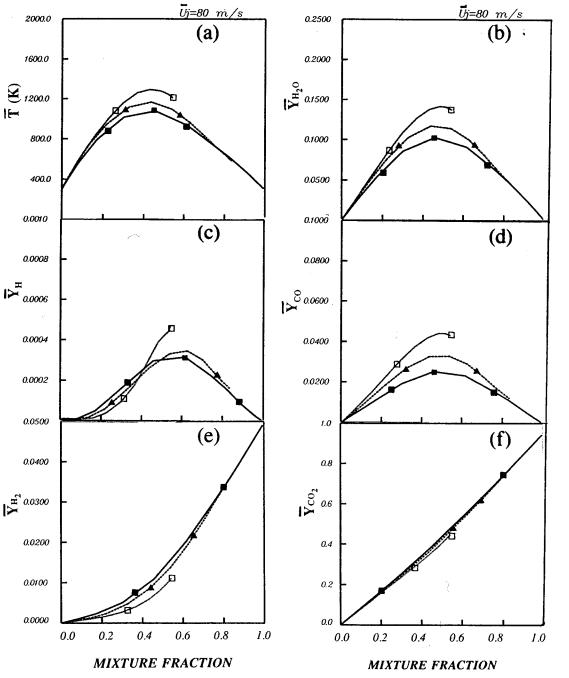

Fig. 7. Radial profiles of mean temperature and the mean mass fractions of H, H_2, H_2O, CO, and CO_2 calculated for various axial locations in the flame with $\bar{U}_j = 80$ m/s and plotted versus mean mixture fraction, $\tilde{\xi}$ at the corresponding radial location. Symbols: ■, ▲, and □ label the profiles at $x/D_j = 6$, 20, and 39, respectively.

locations in the flame with $\overline{U}_j = 80$ m/s and plotted versus the mean mixture fraction, $\tilde{\xi}$, determined at the corresponding radial location. The peak temperature and mass fractions of CO and H_2O increase as x/D_j increases from 6 to 39 and the peaks occur at approximately the same mixture fraction, $\tilde{\xi} \simeq 0.45 - 0.5$ regardless of the axial location. The peak mass fraction of hydrogen radicals occurs at richer mixtures with $\tilde{\xi} \simeq 0.6$ and the peak increases also with increasing x/D_j. The radial profiles of $\overline{Y}_H$ in mixture fraction space is extremely broad covering the full range of $0.1 < \xi < 1.0$. This is not supported by the laminar flame calculations which show narrow profiles of Y_H peaking around stoichiometric mixture fraction [30]. The shift toward lower values of $\overline{Y}_H$ on the lean side of the flame with increasing x/D_j is also interesting and is mainly due to the decreasing penetration of H_2 to the lean side of the flame and hence lower formation rate of H due to reactions ω_{II} and ω_{III}.

A direct comparison between the instantaneous measurements and computations is presented in Figs. 8–11 for two axial locations in the slowly mixing flame with $\overline{U}_j = 130$ m/s. Measured and calculated scatter plots for temperature and the mass fractions of O_2 and CO_2 are shown in Fig. 8 and the mass fractions of H_2, H_2O, and CO are compared in Fig. 9. Both Figs. 8 and 9 refer to $x/D_j = 6$ and are plotted versus mixture fraction, ξ. Excellent qualitative agreement is obtained for all scalars with the calculated peak values of temperature and the mass fractions of H_2O and CO similar to those measured. Within any mixture fraction band, the degree of scatter in both the data and the computations is also similar. Calculations show that the penetration of O_2 to the rich side of the flame is more significant than shown by measurements.

Figures 10 and 11 show comparisons between the measured and calculated scatter plots of temperature and the mass fraction of O_2, CO_2, H_2, H_2O, and CO at $x/D_j = 39$ in the flame with $\overline{U}_j = 130$ m/s. At this downstream axial location mixing rates are less intense resulting in higher peak temperatures and an increase of more than 50% and 30% in the peak levels of CO and H_2O, respectively.

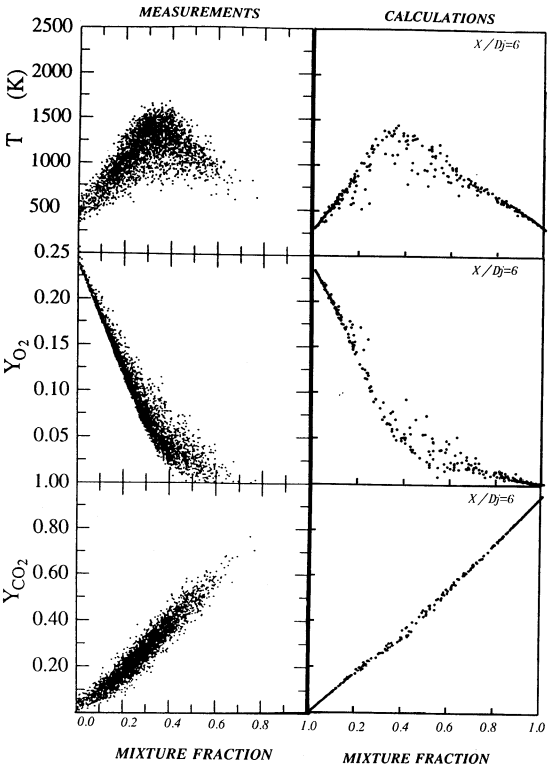

Fig. 8. Measured (left) and calculated (right) scatter plots for temperature and the mass fractions of O_2 and CO_2 plotted versus mixture fraction, ξ for the H_2/CO_2 flame with $\overline{U}_j = 130$ m/s at $x/D_j = 6$.

The calculated peak temperature and the peak mass fractions of CO and H_2O are about 10%–15% lower than the measurements but occur at the same mixture fractions. The oxygen penetration to the rich side is minimal at this axial location but the calculated CO levels on the lean side of stoichiometric are higher than shown experimentally.

A quantitative comparison is presented in Fig. 12 between the averaged measurements and computations for the same flame with $\overline{U}_j = 130$ m/s. Profiles of mean temperature and species mass fractions are plotted versus mean mixture fraction for $x/D_j = 6$ and 39. The peak temperature and mass fraction of water are underestimated while the mass fraction of hydrogen is overestimated in the stoichiometric region around $\xi = 0.37$. This indicates that the overall conversion of fuel hydrogen to water is underestimated, implying that finite rate chemistry effects are stronger in the computed flame. This is consistent with the fact that this

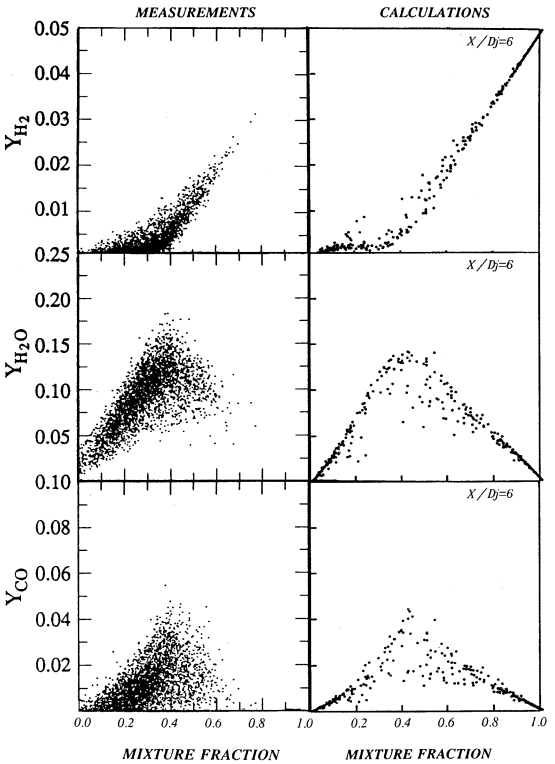

Fig. 9. Measured (left) and calculated (right) scatter plots for the mass fraction of H_2, H_2O, and CO plotted versus mixture fraction, ξ for the H_2/CO_2 flame with $\overline{U}_j$ = 130 m/s at x/D_j = 6.

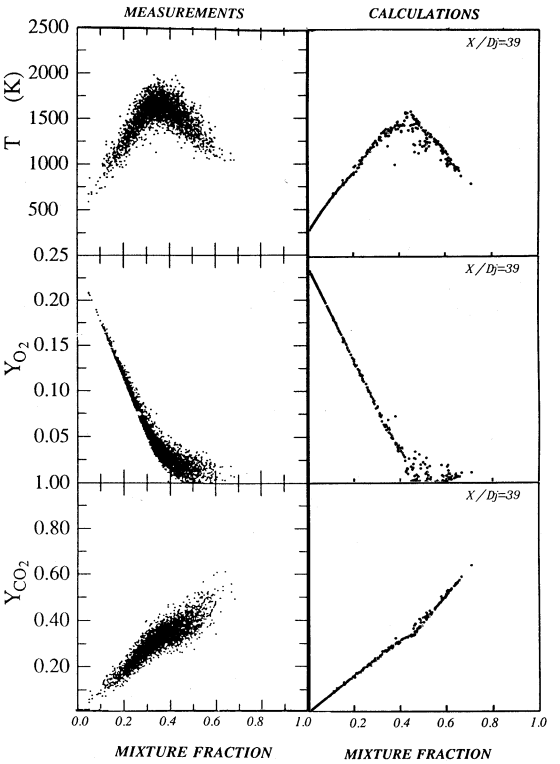

Fig. 10. Measured (left) and calculated (right) scatter plots for temperature and the mass fractions of O_2 and CO_2 plotted versus mixture fraction, ξ for the H_2/CO_2 flame with $\overline{U}_j$ = 130 m/s at x/D_j = 39.

flame is closer to numerical blowoff than the experimental flame. The peak level of CO is in very good agreement at $x/D_j = 6$ but is underpredicted at $x/D_j = 39$. On the lean side of stoichiometric, computations show excessive conversion of CO_2 to CO. This is essentially an artefact of reaction I in the reduced mechanism where the concentrations of CO and CO_2 are balanced only by the water–gas shift reaction.

Intermediate Jet Velocity

Numerical flame blowoff velocity occurs approximately at $\overline{U}_j$ = 220 m/s and the flame with $\overline{U}_j$ = 160 m/s can therefore be considered as intermediate. The results from the calculations of this flame can be compared with the data from the intermediate flame investigated experimentally with $\overline{U}_j$ = 229 m/s. It should be noted that this is only a relative rather than direct comparison between the measured and calculated flame behavior as it approaches extinction.

Calculated scatter plots for temperature are shown in Fig. 13 for a range of axial locations in the flame with $\overline{U}_j$ = 160 m/s. At $x/D_j = 2$, the peak temperature reached is only 1400 K and the scatter is very broad. These are strikingly different results to those presented in Fig. 6 for the flame with $\overline{U}_j$ = 80 m/s. The mixing rates in this flame are more intense and at $x/D_j = 2$ significant mixing, without any chemical reaction, has occurred between the pilot, air and fuel streams. With increasing x/D_j, more chemical reaction is occurring and the peak temperature increases to ~ 1600 K at $x/D_j = 50$. The occurrence of nonreacted or partially reacted fluid samples within the reactive zone also decreases to zero at x/D_j = 50.

Figure 14 shows a comparison between the measurements made in flame $V2$ and computations for the flame with $\overline{U}_j$ = 160 m/s. Scat-

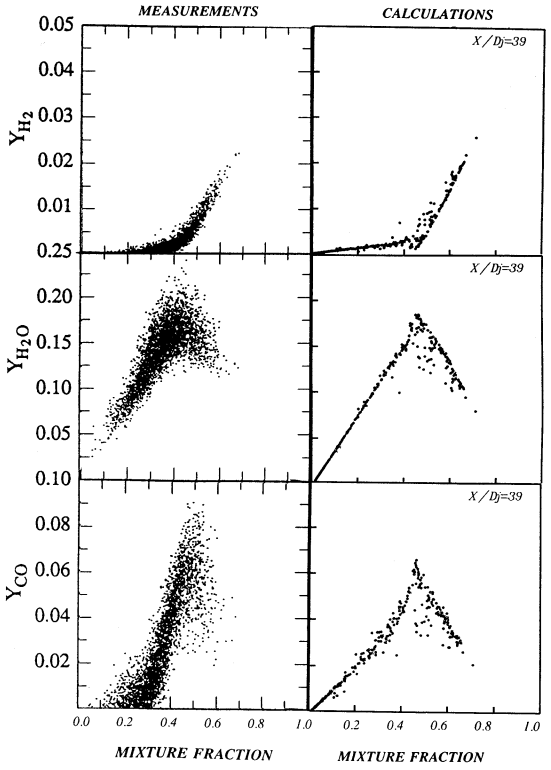

Fig. 11. Measured (left) and calculated (right) scatter plots for the mass fraction of H_2, H_2O, and CO plotted versus mixture fraction, ξ for the H_2/CO_2 flame with $\overline{U}_j$ = 130 m/s at x/D_j = 39.

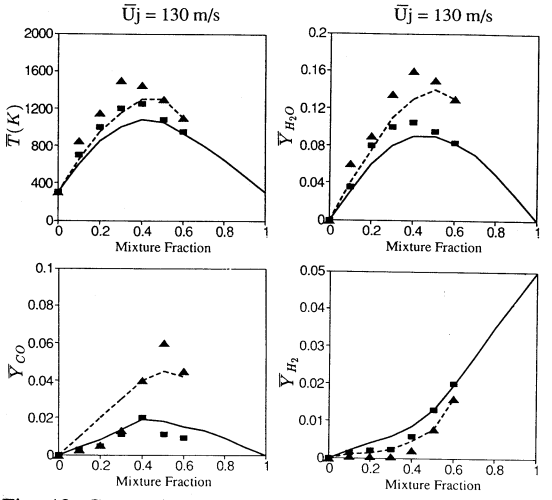

Fig. 12. Comparison between measured and computed mean profiles of temperature and the mass fractions of CO, H_2O, and H_2 at x/D_j = 6 and 39 in the flame with $\overline{U}_j$ = 130 m/s. Symbols refer to experimental data. ——, ■: x/D_j = 6; -----, ▲: x/D_j = 39.

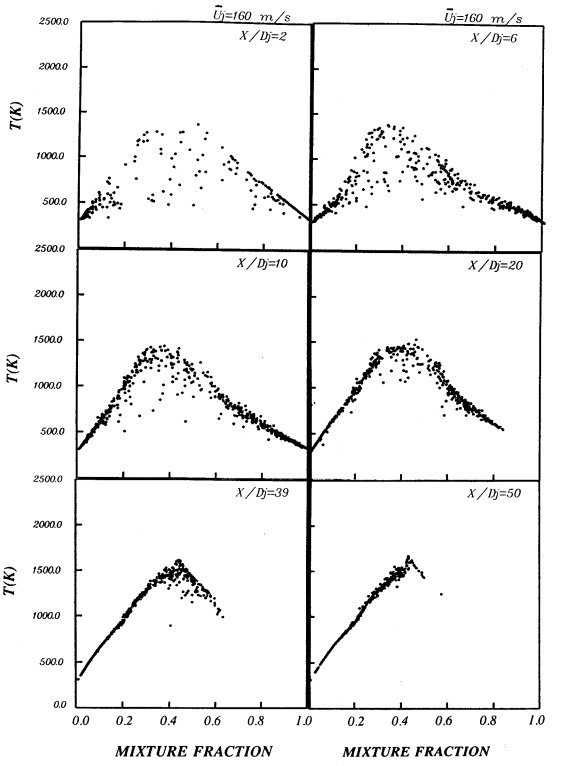

Fig. 13. Calculated scatter plots of temperature versus mixture fraction at various axial locations in a H_2/CO_2 piloted jet flame with $\overline{U}_j$ = 160 m/s.

ter plots for temperature and the mass fractions of H_2O and CO are presented versus mixture fraction for x/D_j = 6. The peak calculated values are generally lower than those measured for temperature as well as Y_{CO} and Y_{H_2O}. The scatter in both the measurements and computations is significant especially for fluid samples within the reactive zone indicating significant departures from chemical equilibrium.

High Jet Velocity

Significant chemical kinetic effects are expected in the flames with $\overline{U}_j$ = 190 m/s and 210 m/s which are closet to blowoff. Figures 15 and 16 show scatter plots for temperature in these flames calculated at various axial locations and plotted versus mixture fraction, ξ. For the flame with $\overline{U}_j$ = 190 m/s, fluid samples simply mix without reaction down to x/D_j = 6 where the peak calculated temperature de-

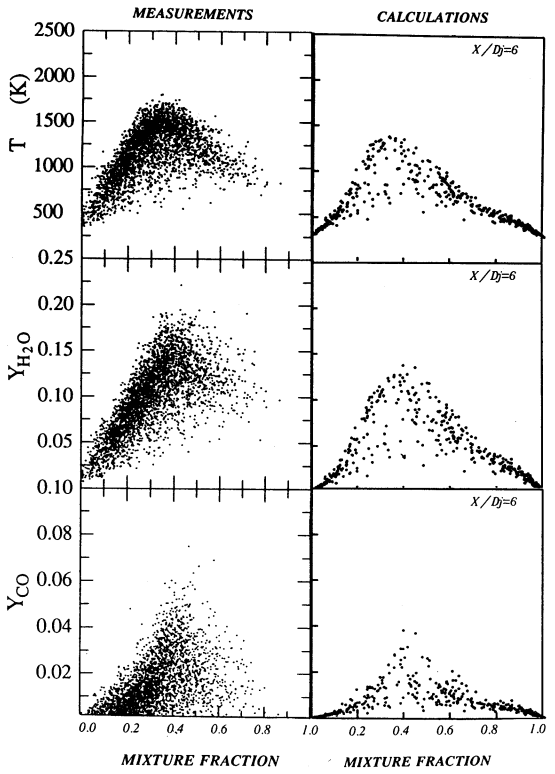

Fig. 14. Measured (left) and calculated (right) scatter plots for temperature and the mass fractions of O_2 and CO_2 plotted versus mixture fraction, ξ for the H_2/CO_2 flame with $\overline{U}_j$ = 160 m/s at x/D_j = 6.

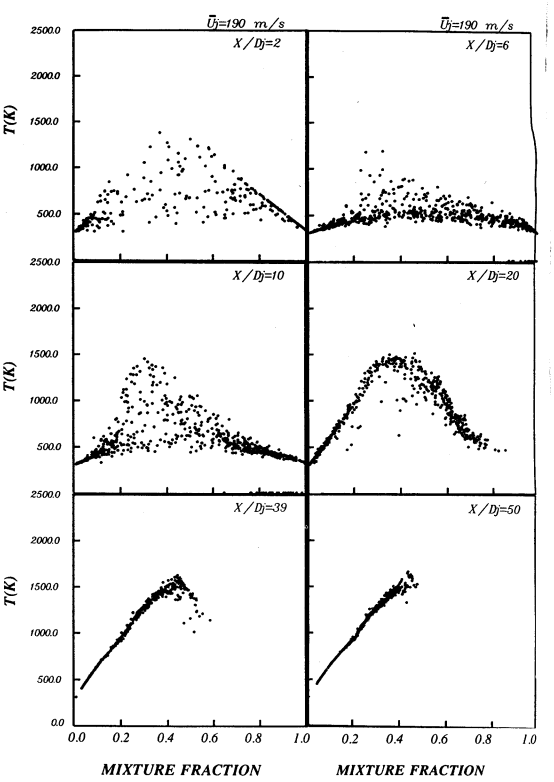

Fig. 15. Calculated scatter plots of temperature versus mixture fraction at various axial locations in a H_2/CO_2 piloted jet flame with $\overline{U}_j$ = 190 m/s.

creases to ~ 1000 K. At x/D_j = 10 some reaction has taken place and the peak temperature has increased to ~ 1500 K but the scatter is still very broad. At x/D_j = 50 all fluid particles within the reaction zone are reacted and the temperature reaches its peak of ~ 1600 K. For the flame with $\overline{U}_j$ = 210 m/s reaction is further delayed to x/D_j = 20 and a significant proportion of fluid samples is still unreacted even at x/D_j = 39. This flame is significantly shorter than the lower velocity flames because it behaves essentially like an unreacted jet.

Discussion

Figure 17 presents six plots, each showing a number of radial profiles of the mean temperature calculated for a range of axial locations in the flames with $\overline{U}_j$ = 80, 130, 160, 190, 210, and 220 m/s. These plots highlight the decrease in the peak temperature at x/D_j = 2, 6 with increasing fuel jet velocity, due to the increase in turbulent mixing and the absence of chemical reaction at these upstream axial locations. Another feature of these plots is that they illustrate the delay in the ignition of fluid particles and the ensuing increase in temperature with

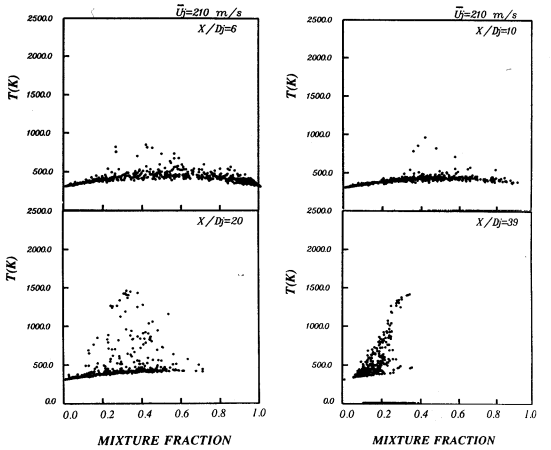

Fig. 16. Calculated scatter plots of temperature versus mixture fraction at various axial locations in a H_2/CO_2 piloted jet flame with $\overline{U}_j$ = 210 m/s.

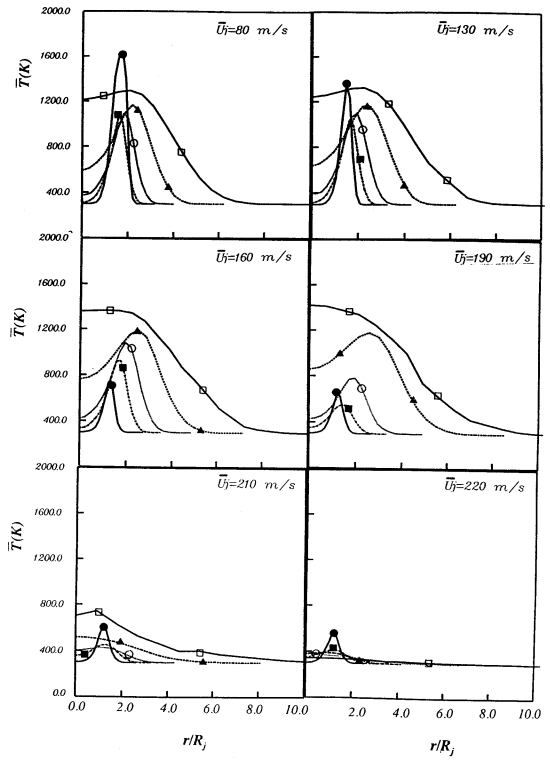

Fig. 17. Radial profiles of the calculated mean temperature at various axial locations for the flames with $\bar{U}_j$ = 80, 130, 160, 190, 210, and 220 m/s. Symbols: ●, ■, ○, ▲, and □ label the profiles at x/D_j = 2, 6, 10, 20, and 9, respectively.

increasing fuel jet velocity. For all flames, the lowest peak temperature occurs at $x/D_j = 6$ and the flame is well ignited by $x/D_j = 10$ except for the flame with $\bar{U}_j = 210$ m/s, where ignition is delayed further and starts to occur at $x/D_j = 20$. The flame with $\bar{U}_j = 220$ m/s is fully extinguished.

Just downstream of the jet exit plane, fluid particles issuing from the hot pilot stream mix with fluid particles from the air and fuel streams. For the low-velocity flames, chemical reaction starts to occur as soon as particles enter the reactive space and this continues further downstream leading to an increase in the peak flame temperature up to the theoretical maximum. With increasing fuel jet velocity, and hence turbulent mixing rates, reaction is delay until further downstream while only mixing occurs in the upstream part of the jet. When reaction is delayed to a point where fluid particles on the jet centerline have mixture fractions outside the reactive zone, ignition will never occur and the flame is extinguished. It is not strictly correct to talk about localized extinction in these computations since what appears to be an extinguished fluid samples within the reactive zone has actually never been ignited. Experiments in pilot-stabilized flames of H_2/CO_2 [30] as well as other fuels [17, 40] show that fluid samples are ignited in the region influenced by the pilot stream. Local extinction occurs downstream of the pilot with increasing fuel jet velocity and reignition occurs further downstream when the turbulent mixing rates are relaxed. Computations presented here do not show significant ignition in the pilot region. This may be partly due to the coarse mixing models used here. This aspect, however, requires further investigation.

CONCLUSIONS

A reduced, three-step chemical mechanism is successfully incorporated in the solution of the joint velocity-composition pdf transport equation, using Monte Carlo methods, for turbulent pilot-stabilized nonpremixed flames of H_2/ CO_2 fuel mixtures. The generation of multidimensional look-up tables and their subsequent use in the computations to determine density, dependent properties, and composition change due to chemical reaction is demonstrated.

Calculations of the velocity, turbulence, and mixing fields are adequate and the computed flame length, radial spread rate, and excess velocity decay on the jet centerline agree with the expected behavior of jet flames. For the flames with low and intermediate jet velocities, where the chemical kinetic effects are small to moderate, the calculated reactive scalars agree with measurements in similar flames. Measured and computed levels of temperature and mass fractions of stable species compare reasonably well.

Deviations between measurements and calculations occur for flames with significant finite rate chemical kinetic effects close to extinction. Calculations show a delay in ignition of fluid particles as mixing rates become more intense while experiments show ignition in the pilot flame region, followed by localized extinc-

tion downstream of the pilot then by reignition further downstream. The computed blowoff velocity is about 20% lower than that obtained experimentally.

Dr. Masri and Mr. Taing are supported by the Australian Research Council. Prof. Pope is supported in part by Grant No. CTS-9113236 from the National Science Foundation.

REFERENCES

1. Liew, S. K., Bray, K. N. C., and Moss, J. B., *Combust. Sci. Technol.* 27:69–73 (1981).
2. Peters, N., *Combust. Sci. Technol.* 30:1–17 (1983).
3. Masri, A. R., Bilger, R. W., and Dibble, R. W., *Combust. Flame* 74:267–284 (1988).
4. Rogg, B., Behrendt, F., and Warnatz, J., *Twenty-First Symposium (International) on Combustion*, The Combustion Institute, Pittsburgh, 1986, pp. 1533–1541.
5. Mauss, F., Keller, D., and Peters, N., *Twenty-Third Symposium (International) on Combustion*, The Combustion Institute, Pittsburgh, 1990, pp. 693–698.
6. Pope, S. B., *Phys. Fluids* 24:588–596 (1981).
7. Pope, S. B., *Prog. Ener. Combust. Sci.* 11:119–192 (1985).
8. Anand, M. S., and Pope, S. B., *Combust. Flame* 67:127–142 (1987).
9. Chen, J. Y., Kollmann, W., and Dibble, R. W., *Combust. Sci. Technol.* 64:315–346 (1989).
10. Chen, J. Y., Dibble, R. W., and Bilger, R. W., *Twenty-Third Symposium (International) on Combustion*, The Combustion Institute, Pittsburgh, 1990, pp. 775–780.
11. Pope, S. B., and Chen, Y. L., *Phys. Fluids A* 2:1437–1449 (1990).
12. Norris, A. T., and Pope, S. B., *Combust. Flame* 83:27–42 (1990).
13. Bilger, R. W., *Phys. Fluids A* 5(2):436–444 (1993).
14. Klimenko, A. Yu., *Fluid Dynamics* 25:327–335 (1990), translated from *Mekh. Zhidkoshi Gaza* 3:3–10 (1990).
15. Smith, N., and Bilger, R. W., *Twenty-Fourth Symposium (International) on Combustion*, The Combustion Institute, Pittsburgh, 1992, pp. 263–269.
16. Masri, A. R., Dibble, R. W., and Bilger, R. W., *Combust. Flame* 71:245–266 (1988).
17. Masri, A. R., Bilger, R. W., and Dibble, R. W., *Combust. Flame* 73:261–286 (1988).
18. Masri, A. R., Dibble, R. W., and Barlow, R. S., *Combust. Flame* 89:167–185 (1992).
19. Stårner, S. H., Bilger, R. W., Dibble, R. W., and Barlow, R. S., *Combust. Flame* 83:63–74 (1991).
20. Stårner, S. H., Bilger, R. W., Dibble, R. W., and Barlow, R. S., *Combust. Sci. Technol.* 72:559–269 (1990).
21. Masri, A. R., Dibble, R. W. and Barlow, R. S., *Twenty-Fourth Symposium (International) on Combustion*, The Combustion Institute, Pittsburgh, 1992, pp. 317–324.
22. Pope, S. B., *Phys. Fluids A* 3:1947–1957 (1991).
23. Correa, S. M., and Pope, S. B., *Twenty-Fourth Symposium (International) on Combustion*, The Combustion Institute, Pittsburgh, 1992, pp. 279–285.
24. Peters, N., *Lect. Notes Phys.* 241:90–109 (1985).
25. Bilger, R. W., Stårner, S. H., and Kee, R. J., *Combust. Flame* 80:135–149 (1990).
26. Smooke, M. D., (Ed.), *Reduced Kinetic Mechanisms and Flames*, Springer, Berlin, 1992.
27. Peters, N., and Rogg, B. (Eds.), *Reduced Kinetic Mechanisms for Applications in Combustion Systems*, Springer, Berlin, 1993.
28. Maas, U. A., and Pope, S. B., *Combust. Flame* 88:239–264 (1992).
29. Maas, U. A., and Pope, S. B., *Twenty-Fourth Symposium (International) on Combustion*, The Combustion Institute, Pittsburgh, 1992, pp. 103–112.
30. Masri, A. R., Dibble, R. W., and Barlow, R. S., *Combust. Flame* 91:285–309 (1992).
31. Pope, S. B., *Prog. Ener. Combust. Sci.* 11:119–192 (1985).
32. Pope, S. B., *Combust. Sci. Technol.* 28:131–135 (1982).
33. Pope, S. B., *AIAA J.* 22:896–904 (1984).
34. Warnatz, J., *Combustion Chemistry* (W. C. Gardiner, Jr., Ed.), Springer, Berlin 1984, p. 197.
35. Rogg, B., and Williams, F. A., *Twenty-Second Symposium (International) on Combustion*, The Combustion Institute, Pittsburgh, 1988, pp. 1441–1451.
36. Masri, A. R., and Pope, S. B., *Combust. Flame* 81:13–29 (1990).
37. Nguyen, T. V., and Pope, S. B., *Combust. Sci. Technol.* 42:13–45 (1984).
38. Masri, A. R., and Bilger, R. W., *Twenty-First Symposium (International) on Combustion*, The Combustion Institute, Pittsburgh, 1986, pp. 1511–1520.
39. Hottel, H. C., and Hawthorne, W. R., *Third Symposium (International) on Combustion*, The Combustion Institute, Pittsburgh, 1949, pp. 254–266.
40. Masri, A. R., and Dibble, R. W., *Twenty-Second Symposium (International) on Combustion*, The Combustion Institute, Pittsburgh, 1988, pp. 607–618.

Received 13 November 1992; revised 20 April 1993